Superextremal spinning black holes via accretion

Tanja Bode,[1] Pablo Laguna,[1] and Richard Matzner[2]

[1]*Center for Relativistic Astrophysics and School of Physics, Georgia Institute of Technology, Atlanta, Georgia 30332, USA*
[2]*Center for Relativity and Department of Physics, University of Texas at Austin, Austin, Texas 78712, USA*

A Kerr black hole with mass M and angular momentum J satisfies the extremality inequality $|J| \leq M^2$. In the presence of matter and/or gravitational radiation, this bound needs to be reformulated in terms of local measurements of the mass and the angular momentum directly associated with the black hole. The isolated and dynamical horizon framework provides such quasilocal characterization of black hole mass and angular momentum. With this framework, it is possible in axisymmetry to reformulate the extremality limit as $|J| \leq 2M_H^2$, with M_H the irreducible mass of the black hole computed from its apparent horizon area and J obtained using a rotational Killing vector field on the apparent horizon. The $|J| \leq 2M_H^2$ condition is also equivalent to requiring a non-negative black hole surface gravity. We present numerical experiments of an accreting black hole that temporarily violates this extremality inequality. The initial configuration consists of a single, rotating black hole surrounded by a thick, shell cloud of negative energy density. For these numerical experiments, we introduce a new matter-without-matter evolution method.

I. INTRODUCTION

Kerr spacetimes, representing a spinning black hole (BH) in isolation, have a bound on the maximum allowed angular momentum. If M is the mass of the BH and J its angular momentum, the bound or *extremality condition* reads $|J| \leq M^2$. An extremal Kerr BH saturates this condition (i.e. $|J| = M^2$). Kerr spacetimes violating the extremality condition (i.e. $|J| > M^2$) have naked singularities instead of BHs. A natural question to ask then is whether more general BH spacetimes (e.g. BHs in the presence of matter, Maxwell fields, gravitational radiation, and/or other BHs) are also subject to extremality conditions, thus precluding the existence of *superextremal* BHs.

The existence of extremality conditions in more general BH spacetimes has been investigated in a series of papers by Ansorg and collaborators. These studies considered axisymmetric and stationary BHs surrounded by matter [1,2]. In some cases, Maxwell fields were also included [3]. Of direct relevance to our work is the study by Ansorg and Petroff [4] demonstrating the feasibility of configurations with superextremal BHs. More recently, in an initial data study of binary BHs with nearly extremal spins [5], each BH was found to have an inner, superextremal apparent horizon (AH), but the outermost (and true) AH was subextremal.

As pointed out by Booth and Fairhurst [6], at the core of any study of BH extremality conditions is characterizing what one means by mass and angular momentum associated with the BH, namely, distinguishing the "local" properties of the BH from those of its environment. As shown also in [6], the natural tools for such a task are those provided by the isolated and dynamical horizon framework [7]. Using this framework, Booth and Fairhurst [6] reformulated extremality conditions in terms of restrictions on

isolated and dynamical horizons, and introduced a parameter that determines how close a horizon is to extremality.

The goal of our work is to investigate the formation of a *superextremal* BH in a dynamical setup using the tools of numerical relativity. Specifically, we consider a subextremal BH surrounded with a spherically symmetric cloud of negative energy density. As the BH accretes the cloud, its mass decreases and its angular momentum increases. As a consequence, the dimensionless spin parameter of the BH increases. This approach to spinning up a BH by decreasing its mass is complementary to the more astrophysically relevant case in which a BH spins up by gaining angular momentum from the material it swallows [8]. For clouds with enough negative energy density, we are able to build superextremal BHs. The superextremal state is, however, not stable. Nonaxisymmetric instabilities develop, triggering emission of gravitational radiation that carried angular momentum.

Our study also introduces a new evolution scheme called matter-without-matter (MWM). The MWM approach consists of evolving the spacetime geometry using the Baumgarte-Shapiro-Shibata-Nakamura (BSSN) [9] evolution equations without their matter source terms, namely, the vacuum version of the evolution equations. The matter fields are constructed at each step from the BSSN constraints (Hamiltonian, momentum, and connection constraints). In addition, the stress-energy tensor is required to have a form for which the matter source terms in the BSSN evolution equations vanish. The approach is reminiscent of the constraint-violating BH initial data evolved in a previous study [10]. Our MWM method differs, however, from work with hydro-without-hydro evolutions [11,12]. In those studies, the matter hydrodynamics was preprescribed and was used as input to construct the source terms in the evolution equations.

The paper is organized as follows. In Sec. II, we summarize the extremality conditions and discuss the condition used in our numerical experiments to identify the emergence of superextremality. Section III describes the MWM evolution approach and the conditions that the matter content must satisfy. In Sec. IV, we describe the initial data configurations used in our simulations. Results showing the formation of a superextremal BH are given in Sec. V. In Sec. VI, we address the degree to which the null-energy condition is satisfied by our spacetimes. In Sec. VII, we investigate the late-time behavior in terms of the constraints. Conclusions are presented in Sec. VIII. The numerical simulations and results were obtained with the MAYA code as described in Refs. [10,13,14]. Subscripts $a, b, c, \ldots$ will denote spacetime indices while $i, j, k, \ldots$ will denote spatial indices. We use units in which $G = c = 1$.

II. EXTREMALITY CONDITIONS

There are three notions of extremality in stationary, asymptotically flat BH spacetimes (see [6] for details): (i) the angular momentum J and mass M of a BH satisfy the bound $\chi \equiv |J|/M^2 \leq 1$; (ii) the surface gravity κ of a BH satisfies the bound $\kappa \geq 0$; and (iii) the interior of a nonextremal BH contains trapped surfaces, while there are no trapped surfaces in the interior of an extremal BH.

The first notion of extremality ($\chi \leq 1$) compares the Christodoulou mass [15] M to the angular momentum J of the BH. The Christodoulou mass is given by

$$M^2 \equiv M_H^2 + \frac{J^2}{4M_H^2} = M_H^2 \left[1 + \left(\frac{J}{2M_H^2} \right)^2 \right]. \quad (1)$$

M_H is a local measure of the BH mass, called the irreducible mass. The mass is computed from $M_H = \sqrt{A/16\pi}$, with A the area of the AH of the BH. The angular momentum J is also obtained locally using rotational Killing vectors on the AH [7].

The surface gravity κ of stationary and axisymmetric BHs is obtained from $k^b \nabla_b k^a = \kappa k^a$, where k^a describes the Killing vector that becomes null at the horizon. For Kerr spacetimes, the surface gravity takes the form

$$\kappa = \frac{1}{2M_H} \frac{(1-\chi^2)^{1/2}}{[1 + (1-\chi^2)^{1/2}]}. \quad (2)$$

Evident from Eq. (2) is the equivalence between the first two notions of extremality, namely $\chi \leq 1$ and $\kappa \geq 0$.

The goal of our study is to investigate conditions under which the extremality conditions $\chi \leq 1$ and $\kappa \geq 0$ are violated. Using χ for this purpose has, however, the following drawback. From Eq. (1), it is not difficult to show that

$$\left(\frac{2M_H^2}{M^2} - 1 \right)^2 = 1 - \frac{J^2}{M^4} = 1 - \chi^2. \quad (3)$$

Thus, by construction $\chi \leq 1$. It has been then suggested [5,6] that a quantity more suitable to investigate extremality is $\zeta \equiv |J|/(2M_H^2)$, or equivalently $\zeta \equiv 8\pi|J|/A$ [16]. In terms of ζ, the spin parameter χ and the surface gravity κ take the form

$$\chi = 1 - \frac{(1-\zeta)^2}{1+\zeta^2}, \quad (4)$$

$$\kappa = \frac{1-\zeta^2}{4M}, \quad (5)$$

respectively. Thus, for $\zeta \leq 1$, one recovers the extremality conditions $\chi \leq 1$ and $\kappa \geq 0$. The advantage of the new spin parameter ζ is that values $\zeta > 1$ are allowable. Furthermore, for $\zeta > 1$, one still has $\chi \leq 1$, but the surface gravity, on the other hand, becomes negative.

In Ref. [6], a new notion of extremality was introduced in terms of ζ: A BH is said to be *subextremal* if $\zeta < 1$ ($\kappa > 0$), *extremal* if $\zeta = 1$ ($\kappa = 0$), and *superextremal* if $\zeta > 1$ ($\kappa < 0$). This new notion of extremality is derived assuming that: (i) the spacetime is axisymmetric; (ii) the null energy condition is satisfied; and (iii) the cross sections of the horizon are embeddable in Euclidean $\mathbb{R}^3$. A generalization of extremality, relaxing the axisymmetry and embeddability assumptions but keeping the null energy condition, is also possible [6].

III. MATTER-WITHOUT-MATTER EVOLUTIONS

Our study introduces also an evolution scheme that we call the *matter-without-matter* method. Under the MWM approach, the geometry of the spacetime is evolved using the vacuum or source-free BSSN evolution equations. There is no need for matter evolution equations. As we shall show next, the matter fields are obtained at every step of the evolution from the BSSN constraints (Hamiltonian, momentum, and connection constraints) together with *equations of state*. To demonstrate how the MWM works, we will rederive the BSSN evolution equations, taking explicitly into account a matter content that is *invisible* to these equations.

The BSSN formulation of the Einstein equations consists of a set of evolution equations for the conformal metric $\tilde{\gamma}_{ij}$, the conformal factor ϕ, the trace of the physical extrinsic curvature K, the trace-free part of the conformal extrinsic curvature $\tilde{A}_{ij}$, and the connection $\tilde{\Gamma}^i \equiv \tilde{\gamma}^{jk}\tilde{\Gamma}^i_{jk} = -\partial_j\tilde{\gamma}^{ij}$ (see Ref. [17] for details). The evolution equations for ϕ, $\tilde{\gamma}_{ij}$, and K are, respectively,

$$\partial_o \phi = -\frac{1}{6}\alpha K, \quad (6)$$

$$\partial_o \tilde{\gamma}_{ij} = -2\alpha \tilde{A}_{ij}, \quad (7)$$

$$\partial_o K = -\nabla_i \nabla^i \alpha + \alpha\left(\tilde{A}^{ij}\tilde{A}_{ij} + \frac{1}{3}K^2\right) + 4\pi\alpha(\rho + S). \quad (8)$$

∇ denotes covariant differentiation with respect to the physical metric $\gamma_{ij} = e^{4\phi}\tilde{\gamma}_{ij}$, α is the lapse function, and β^i is the shift vector; we define $\partial_o \equiv \partial_t - \mathcal{L}_\beta$, with $\mathcal{L}_\beta$ the spatial Lie derivative along β^i. Above, the source terms ρ and $S = \gamma^{ij}S_{ij}$ are obtained from

$$\rho = n^a n^b T_{ab}, \quad (9)$$

$$j^i = -\gamma^{ia}n^b T_{ab}, \quad (10)$$

$$S_{ij} = \gamma_i^a \gamma_j^b T_{ab}, \quad (11)$$

with T_{ab} the stress-energy tensor and with n^a the unit, timelike normal to the constant t hypersurfaces. That is, the stress-energy tensor has the following form:

$$T_{ab} = \rho n_a n_b + 2j_{(a}n_{b)} + S_{ab}. \quad (12)$$

Before considering the evolution equations for $\tilde{A}_{ij}$ and $\tilde{\Gamma}^i$, we need to recall the constraints in the BSSN formulation. As with any $3 + 1$ formulation of the Einstein field equations of general relativity, the BSSN formulation involves the Hamiltonian and momentum constraints. In terms of the BSSN variables, these constraints read

$$e^{-5\phi}\tilde{\nabla}_i\tilde{\nabla}^i e^\phi - \frac{e^{-4\phi}}{8}\tilde{R} + \frac{1}{8}\tilde{A}^{ij}\tilde{A}_{ij} - \frac{1}{12}K^2 = -2\pi\rho \quad (13)$$

and

$$e^{-6\phi}\tilde{\nabla}_j(e^{6\phi}\tilde{A}^{ij}) - \frac{2}{3}\tilde{\nabla}^i K = 8\pi j^i, \quad (14)$$

respectively. In addition, the BSSN formulation introduces the following new constraints:

$$\mathcal{A} = \tilde{A}^i_i = 0, \quad (15)$$

$$\mathcal{S} = \tilde{\gamma} - 1 = 0, \quad (16)$$

$$\mathcal{G}^i = \tilde{\Gamma}^i + \partial_j\tilde{\gamma}^{ij} = 0. \quad (17)$$

Our MAYA code actively imposes the trace-free (15) and unit-determinant (16) constraints. On the other hand, in numerical evolutions, the Hamiltonian (13), momentum (14), and connection (17) constraints are not explicitly imposed. One of the main virtues of the BSSN formulation is precisely that aspect. Namely, in the course of a BSSN evolution, the constraints (13), (14), and (17) are preserved within tolerable levels. In our MWM scheme, the Hamiltonian, momentum, and connection constraints play a different role. The Hamiltonian and momentum constraints are used to construct ρ and j^i, respectively. But more importantly, in MWM simulations (see below), $\mathcal{G}^i$ evolves away from $\mathcal{G}^i = 0$ and provides a key ingredient in determining the dynamics of the matter content.

For this reason, we need next to rederive the evolution equations for $\tilde{A}_{ij}$ and $\tilde{\Gamma}^i$ without imposing the $\mathcal{G}^i = 0$ constraint.

For the $\tilde{A}_{ij}$ evolution equation, the only place where $\mathcal{G}^i$ enters is in the Ricci tensor R_{ij}, which is normally computed from $R_{ij} = \tilde{R}_{ij} + R_{ij}^\phi$ with

$$\tilde{R}_{ij} = -\frac{1}{2}\tilde{\gamma}^{lm}\partial_l\partial_m\tilde{\gamma}_{ij} + \tilde{\gamma}^{lm}(2\tilde{\Gamma}^k_{l(i}\tilde{\Gamma}_{j)km} + \tilde{\Gamma}^k_{im}\tilde{\Gamma}_{klj})$$
$$+ \tilde{\gamma}_{k(i}\partial_{j)}\tilde{\Gamma}^k + \tilde{\Gamma}^k\tilde{\Gamma}_{(ij)k}, \quad (18)$$

and

$$R_{ij}^\phi = -2(\tilde{\nabla}_i\tilde{\nabla}_j\phi + \tilde{\gamma}_{ij}\tilde{\nabla}_k\tilde{\nabla}^k\phi) + 4(\tilde{\nabla}_i\phi\tilde{\nabla}_j\phi - \tilde{\gamma}_{ij}\tilde{\nabla}_k\phi\tilde{\nabla}^k\phi), \quad (19)$$

respectively. If $\mathcal{G}^i \neq 0$, the Ricci tensor $\tilde{R}_{ij}$ acquires an additional term, namely,

$$\tilde{R}_{ij} \rightarrow \tilde{R}_{ij} = -\frac{1}{2}\tilde{\gamma}^{lm}\partial_l\partial_m\tilde{\gamma}_{ij} + \tilde{\gamma}^{lm}(2\tilde{\Gamma}^k_{l(i}\tilde{\Gamma}_{j)km} + \tilde{\Gamma}^k_{im}\tilde{\Gamma}_{klj})$$
$$+ \tilde{\gamma}_{k(i}\partial_{j)}\tilde{\Gamma}^k + \tilde{\Gamma}^k\tilde{\Gamma}_{(ij)k} - \tilde{\gamma}_{k(i}\partial_{j)}\mathcal{G}^k - \mathcal{G}^k\tilde{\Gamma}_{(ij)k}. \quad (20)$$

Therefore, R_{ij} is given instead as $R_{ij} = \tilde{R}_{ij} + R_{ij}^\phi + 8\pi M_{ij}$ with $\tilde{R}_{ij}$ and R_{ij}^ϕ given by (18) and (19), respectively, and

$$M_{ij} \equiv -\frac{1}{8\pi}(\tilde{\gamma}_{k(i}\partial_{j)}\mathcal{G}^k + \mathcal{G}^k\tilde{\Gamma}_{(ij)k}). \quad (21)$$

With M_{ij} viewed as an additional source term, one can follow the standard BSSN derivation [17] of the evolution equation for $\tilde{A}_{ij}$ and arrive at

$$\partial_o\tilde{A}_{ij} = e^{-4\phi}[-\nabla_i\nabla_j\alpha + \alpha R_{ij} - 8\pi\alpha(S_{ij} - M_{ij})]^{TF}$$
$$+ \alpha(K\tilde{A}_{ij} - 2\tilde{A}_{ik}\tilde{A}^k_j), \quad (22)$$

where TF denotes the trace-free part of the tensor.

The remaining equation to consider is the evolution equation for $\tilde{\Gamma}^i$. Once again, we will derive this equation without the assumption that the constraint $\mathcal{G}^i = 0$ holds. The starting point is the time derivative of $\tilde{\Gamma}^i = -\partial_j\tilde{\gamma}^{ij} + \mathcal{G}^i$,

$$\partial_t\tilde{\Gamma}^i = -\partial_j\partial_t\tilde{\gamma}^{ij} + \partial_t\mathcal{G}^i. \quad (23)$$

On the other hand, from Eq. (7),

$$\partial_t\tilde{\gamma}^{ij} = 2\alpha\tilde{A}^{ij} + \beta^k\partial_k\tilde{\gamma}^{ij} - \tilde{\gamma}^{ik}\partial_k\beta^j - \tilde{\gamma}^{jk}\partial_k\beta^i + \frac{2}{3}\tilde{\gamma}^{ij}\partial_k\beta^k, \quad (24)$$

which after differentiation reads

$$\partial_t \partial_j \tilde{\gamma}^{ij} = \partial_j (2\alpha \tilde{A}^{ij}) + \beta^k \partial_k \partial_j \tilde{\gamma}^{ij} - \partial_j \tilde{\gamma}^{jk} \partial_k \beta^i$$
$$+ \frac{2}{3} \partial_j \tilde{\gamma}^{ij} \partial_k \beta^k - \tilde{\gamma}^{jk} \partial_j \partial_k \beta^i - \frac{1}{3} \tilde{\gamma}^{ij} \partial_j \partial_k \beta^k. \tag{25}$$

Thus, Eq. (23) becomes

$$\partial_t \tilde{\Gamma}^i = -2\tilde{A}^{ij} \partial_j \alpha - 2\alpha \partial_j \tilde{A}^{ij} - \beta^k \partial_k \partial_j \tilde{\gamma}^{ij} + \partial_j \tilde{\gamma}^{jk} \partial_k \beta^i$$
$$- \frac{2}{3} \partial_j \tilde{\gamma}^{ij} \partial_k \beta^k + \tilde{\gamma}^{jk} \partial_j \partial_k \beta^i + \frac{1}{3} \tilde{\gamma}^{ij} \partial_j \partial_k \beta^k + \partial_t \mathcal{G}^i. \tag{26}$$

Next we use the momentum constraint (14) to eliminate the term involving $\partial_j \tilde{A}^{ij}$, and rewrite (26) as

$$\partial_t \tilde{\Gamma}^i = -2\tilde{A}^{ij} \partial_j \alpha - 16\pi\alpha \tilde{\gamma}^{ij} j_j - 2\alpha \Big(-\tilde{\Gamma}^i_{jk} \tilde{A}^{jk}$$
$$- 6\tilde{A}^{ij} \partial_j \phi + \frac{2}{3} \tilde{\gamma}^{ij} \partial_j K \Big) - \beta^k \partial_k \partial_j \tilde{\gamma}^{ij}$$
$$+ \partial_j \tilde{\gamma}^{jk} \partial_k \beta^i - \frac{2}{3} \partial_j \tilde{\gamma}^{ij} \partial_k \beta^k + \tilde{\gamma}^{jk} \partial_j \partial_k \beta^i$$
$$+ \frac{1}{3} \tilde{\gamma}^{ij} \partial_j \partial_k \beta^k + \partial_t \mathcal{G}^i. \tag{27}$$

With the help of $\partial_j \tilde{\gamma}^{ij} = -\tilde{\Gamma}^i + \mathcal{G}^i$, we obtain

$$\partial_t \tilde{\Gamma}^i = -2\tilde{A}^{ij} \partial_j \alpha - 16\pi\alpha \tilde{\gamma}^{ij} j_j - 2\alpha \Big(-\tilde{\Gamma}^i_{jk} \tilde{A}^{jk}$$
$$- 6\tilde{A}^{ij} \partial_j \phi + \frac{2}{3} \tilde{\gamma}^{ij} \partial_j K \Big) + \beta^j \partial_j \tilde{\Gamma}^i - \tilde{\Gamma}^j \partial_j \beta^i$$
$$+ \frac{2}{3} \tilde{\Gamma}^i \partial_j \beta^j - \beta^j \partial_j \mathcal{G}^i + \mathcal{G}^j \partial_j \beta^i - \frac{2}{3} \mathcal{G}^i \partial_j \beta^j$$
$$+ \tilde{\gamma}^{jk} \partial_j \partial_k \beta^i + \frac{1}{3} \tilde{\gamma}^{ij} \partial_j \partial_k \beta^k + \partial_t \mathcal{G}^i, \tag{28}$$

which can be rewritten as

$$\partial_o \tilde{\Gamma}^i = -2\tilde{A}^{ij} \partial_j \alpha - 2\alpha \Big(-\tilde{\Gamma}^i_{jk} \tilde{A}^{jk} - 6\tilde{A}^{ij} \partial_j \phi + \frac{2}{3} \tilde{\gamma}^{ij} \partial_j K \Big)$$
$$+ \tilde{\gamma}^{jk} \partial_j \partial_k \beta^i + \frac{1}{3} \tilde{\gamma}^{ij} \partial_j \partial_k \beta^k + \partial_o \mathcal{G}^i - 16\pi\alpha \tilde{\gamma}^{ij} j_j, \tag{29}$$

with both $\tilde{\Gamma}^i$ and $\mathcal{G}^i$ treated as vector densities of weight 2/3. Equations (6)–(8), (13), (14), (22), and (29) constitute the basis of our MWM method.

From the form of the stress-energy tensor (12), we see that without any further assumptions, our set of equations is not able to determine S_{ij}. The essence of a MWM evolution is then to impose that matter evolves in such a way that the source terms in (8), (22), and (29) vanish, namely,

$$\rho + S = 0, \tag{30}$$

$$(S_{ij} - M_{ij})^{TF} = 0, \tag{31}$$

$$\partial_o \mathcal{G}^i - 16\pi\alpha e^{-4\phi} j^i = 0. \tag{32}$$

These conditions imply that the stress-energy tensor (12) takes the following form:

$$T_{ab} = \rho \Big(n_a n_b - \frac{1}{3} \gamma_{ab} \Big) + 2 j_{(a} n_{b)} + \gamma^i_a \gamma^j_b M^{TF}_{ij}. \tag{33}$$

The obvious advantage of the MWM method is the direct use of a vacuum (e.g. black hole) BSSN evolution code to construct the spacetime geometry. The matter fields ρ, j^i, and $\mathcal{G}^i$ are obtained after every step from the Hamiltonian (13), momentum (14), and connection (17) constraints. Since the MWM method can be also viewed as evolving constraint-violating data, there are no guarantees that the method is capable of producing stable evolutions. A general proof of the conditions that the initial data have to satisfy in order for the MWM to yield stable evolutions is beyond the scope of this study. We have found, however, that the set of configurations and evolutions for the present study on superextremality were all numerically stable.

IV. INITIAL SETUP

Our study consists of a single, spinning BH puncture [18] enclosed by a thick, spherically symmetric, shell cloud of (in most cases negative) energy density. The shell surrounding the BH has a Gaussian profile and is initially static, with stress-energy tensor given by $T_{ab} = \rho(n_a n_b - \gamma_{ab}/3)$. Specifically, with this choice of stress-energy tensor, initially $j^i = \mathcal{G}^i = \partial_o \mathcal{G}^i = 0$.

Vanishing j^i implies that the momentum constraint reduces to the vacuum case. One can thus directly use the Bowen and York extrinsic curvature solutions for a spinning puncture [19],

$$\hat{A}_{ij} = -\frac{3}{r^3} (\epsilon_{ilk} \hat{r}_j + \epsilon_{jlk} \hat{r}_i) \hat{r}^i J^k, \tag{34}$$

with $\hat{r}^i$ the radial unit vector and J^i the puncture's angular momentum. Constructing initial data requires then solving only the Hamiltonian constraint [20]

$$\Delta \psi + \frac{1}{8} \psi^{-7} \tilde{A}_{ij} \tilde{A}^{ij} + 2\pi \psi^5 \rho = 0, \tag{35}$$

with $\hat{A}_{ij}$ given by (34) and Δ the flat Laplacian. Notice that the standard assumptions of conformal flatness and vanishing trace of the extrinsic curvature have been used. Once a solution to Eq. (35) is found, the initial data for the spatial metric and the extrinsic curvature are obtained from $\gamma_{ij} = \psi^4 \eta_{ij}$ and $K_{ij} = \psi^{-2} \tilde{A}_{ij}$, respectively.

To solve Eq. (35), we use the puncture ansatz $\psi = 1 + m_p/(2r) + u$, with m_p the puncture's bare mass parameter. We choose the source ρ as

$$\rho = \rho_o e^{-(r-r_o)^2/\sigma^2}\left(1 + \frac{m_p}{2r}\right)^{-5}, \qquad (36)$$

and the bare angular momentum as $J^i = J\hat{z}^i$. For all our simulations, we set $J = 0.8$. The last factor in (36) is needed for regularity at the location of the puncture. Thus, Eq. (35) becomes

$$\Delta u + \frac{18}{8}\frac{J^2 r \sin^2\theta}{(r + m_p/2 + ur)^7}$$

$$+ 2\pi\left(\frac{r + m_p/2 + ur}{r + m_p/2}\right)^5 \rho_o e^{-(r-r_o)^2/\sigma^2} = 0, \qquad (37)$$

with $\hat{r}^i\hat{z}^j\eta_{ij} = \cos\theta$.

The parameters r_o and σ are chosen to favor the accretion of most of the shell by the BH in evolution time scales of $\lesssim 40M$. The energy density amplitude parameter ρ_o is the *knob* that controls the mass associated with the shell, and thus regulates the total Arnowitt-Deser-Misner (ADM) mass M_o in the initial data.

Our approach to breaking the extremality bound $\zeta \equiv |J|/(2M_H^2)$ is to not only increase the angular momentum J of the BH, but most importantly to decrease its mass M_H. To accomplish this, we endow the shell surrounding the BH with a negative mass, which decreases the BH's mass as it gets accreted.

It should be noted that in isolation any spinning puncture that models a rotating BH has a small ($\lesssim 0.1\%$ of the total energy) spurious amount of gravitational radiation. This spurious radiation carries away a burst of angular momentum [21]; this amount, however, is small and does not affect the conclusions from our numerical experiment.

Table I shows the parameters used for our simulations: the shell parameters (r_o, σ, ρ_o) and the puncture mass m_p. These quantities and further results are given in dimensionless units in terms of the ADM mass M_o. The last column in Table I reports for each simulation the total spin parameter $\chi_o \equiv J_o/M_o^2$, with J_o the total ADM angular momentum. Since χ_o is associated with the ADM mass and angular momentum of the spacetime, it is not subject to an extremality condition. In particular, χ_o includes

TABLE I. Initial parameters defining the matter shell (r_o, σ, ρ_o). The last two columns display the puncture mass parameter m_p and ADM spin parameter $\chi_o = J_o/M_o^2$. All parameters are given in units of the ADM mass M_o.

Run	r_o/M_o	σ/M_o	$\rho_o M_o^2$	m_p/M_o	χ_o
V0	-	-	0	0.62	0.80
V1	0.88	0.88	$+7.03 \times 10^{-3}$	0.55	0.62
V2	1.03	1.03	-3.77×10^{-4}	0.64	0.85
V3	1.07	1.07	-1.05×10^{-3}	0.71	0.90
V4	1.18	1.18	-1.72×10^{-3}	0.72	1.12
V5	1.23	1.23	-2.00×10^{-3}	0.76	1.20

TABLE II. Initial irreducible mass M_H, Christodoulou mass M, dimensionless spin parameters $\chi = J/M^2$ and $\zeta = |J|/(2M_H^2) = 8\pi|J|/A$, and surface gravity κ of the BH in units of the total ADM mass M_o.

Run	M_H/M_o	M/M_o	χ	ζ	κM_o
V0	0.886	0.994	0.810	0.511	0.209
V1	0.794	0.886	0.796	0.496	0.237
V2	0.908	1.021	0.814	0.515	0.202
V3	0.958	1.071	0.800	0.499	0.196
V4	1.020	1.156	0.830	0.533	0.175
V5	1.056	1.120	0.835	0.538	0.168

angular momentum from outside the horizon. Notice that case V0 consists of a single puncture in vacuum. This case is used as a control run. Case V1 is a fiducial evolution with a *positive* energy density shell. Cases V2–V5 contain shells with increasingly negative energy density. They are the central piece of our study. Table II gives the initial values for the irreducible M_H and Christodoulou M masses for each case. The table also shows the initial values of the BH's spin parameters $\chi = J/M^2$, $\zeta = |J|/(2M_H^2)$, and its surface gravity κ.

Although we are dealing with a single BH, the numerical simulations are challenging. As the BH approaches extremality, the horizon undergoes extreme pancake-like deformation. Because of this severe deformation, in order to capture the dynamics in the vicinity of the BH and to have a chance of locating its AH, we were forced to use meshes with $104^2 \times 52$ grid point shapes, and resolutions in the finest mesh of at least $M/200$, in addition to using sixth-order accurate finite differencing. For some of the cases, we carried out simulations with resolutions of $M/167$ in the finest mesh to investigate the dependence of our results with resolution. We did not find noticeable differences regarding the onset of superextremality. Resolution effects were mostly visible in tracking the AH.

V. SUPEREXTREMAL BLACK HOLES

We evolved the series of runs described in Table I. As previously stated, the V0 case is a control simulation to show that in the absence of matter, the BH mass and angular momentum indeed remain constant. For all the nonvacuum cases, the shell is absorbed early in the evolution. As a consequence, the mass M_H of the BH changes, increasing for the positive energy case V1 and decreasing for the remaining negative energy cases V2–V5.

The case V1 involving a positive energy density shell demonstrates an important feature of our data: The shell of matter has negative angular momentum and positive mass (see Fig. 1). The BH mass increases and the spin decreases as the shell is absorbed. (The time axis in all figures is given in units of the initial Christodoulou mass of the BH.) Figure 1 also shows the behavior of the BH mass and
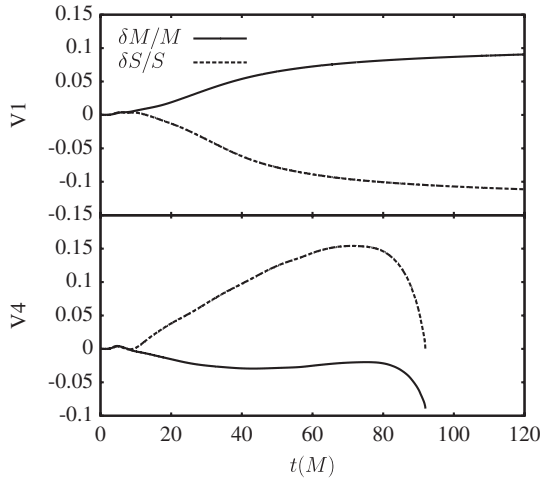
FIG. 1. Fractional change of the Christodoulou mass (solid line) and spin (dashed line) for the cases of V1 (top) and V4 (bottom).

FIG. 2. Modes (2, 0) and (2, 2) of the Weyl scalar Ψ_4 for all cases in the first $120M$ of evolution time.

FIG. 3. Modes (2, 0) and (2, 2) of the Weyl scalar Ψ_4 for all cases after $150M$ of evolution time.

angular momentum for the V4 case with a negative energy shell. The equivalence principle indicates that motion of test bodies is independent of their mass (even the sign of their mass) [22]. While our shells are not test bodies, we do expect the motion of the shells for the V1 positive mass case and the V4 negative mass case to be similar. We thus anticipate and find, for example in V4, that as the negative mass shell falls into the BH, the BH mass *decreases* and the BH angular momentum *increases* (see Fig. 1), thus indicating that our negative energy shells have initially *positive* angular momentum.

As noted before, for all cases regardless of the energy density sign, we have chosen a matter configuration that is axisymmetric. However, as the matter spirals in and is swallowed by the BH, axisymmetry is not preserved. In the next section we will show evidence of nonaxisymmetric accretion. This accretion, however, is ineffective at triggering deformations in the BH horizon. The BH horizon remains for practical purposes axisymmetric, and thus we are able to define a rotational Killing vector to compute the spin. Nevertheless, the deformations on the BH are large enough to allow for gravitational wave emission. The first emission occurs early on around $t \sim 40M$. This is due to the spurious gravitational radiation in spinning punctures mentioned in the previous section. Details of this emission can be seen in Fig. 2 where we show the (2, 0) and (2, 2) modes of the Weyl scalar Ψ_4. Around $t \sim 60M$, the nonaxisymmetric deformations from the accretion trigger a larger burst of gravitational radiation followed by quasinormal ringing (see top panel of Fig. 2). Notice from the bottom panel of Fig. 2 that the (2, 2) mode, which could potentially carry angular momentum, is slightly stronger for the V4 and V5 cases. At late times, $t > 150M$, nonaxisymmetric instabilities trigger a much stronger additional burst of radiation for those two cases,
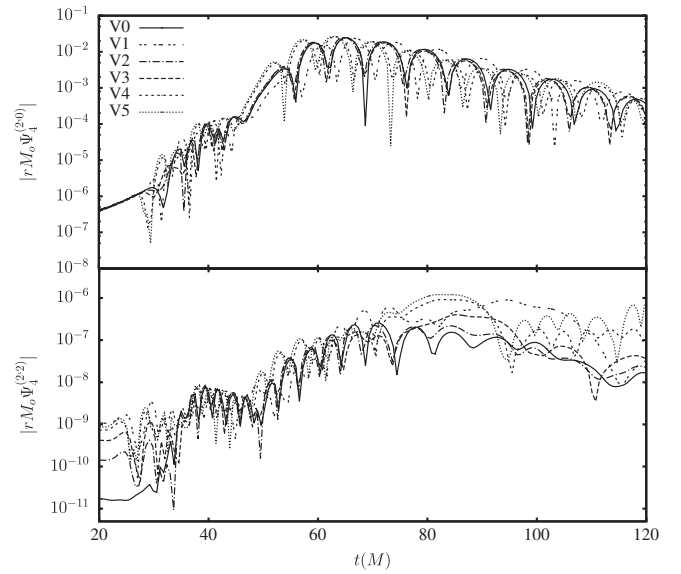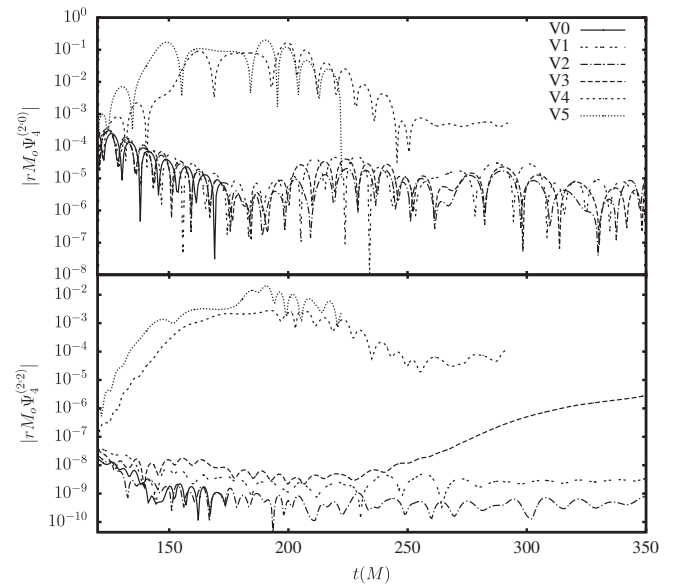
as seen in Fig. 3. As a consequence, the BH loses angular momentum.

Figure 4 shows the core of our study, namely, the evolution of the spin parameter ζ during the spacetime evolution. As expected, ζ is constant in the V0 case. Also expected in case V1, with a positive energy density shell, is the decrease of the spin parameter ζ of the BH due to the monotonic increase (decrease) of its mass (spin) observed in Fig. 1.
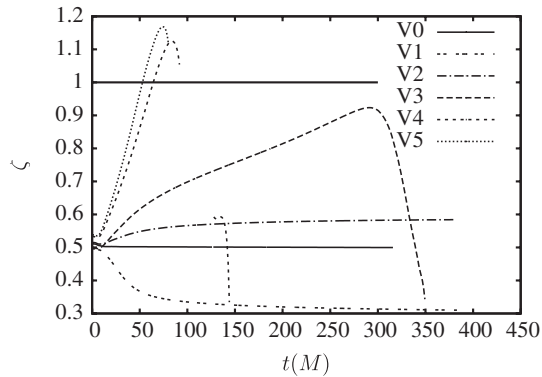
FIG. 4.   Spin parameter ζ as a function of evolution time.

Cases V2–V5, with their negative energy density shells, are our main focus. As the shell is swallowed, the mass of the BH decreases monotonically since it accretes negative mass. Furthermore, given that our negative energy shells have positive angular momentum, the spin of the BH will monotonically increase during the accretion. When taken together, the increase in spin and decrease in mass yield the observed growth of ζ in Fig. 4. Notice from Fig. 4 that the larger the negative energy density of the shell, the faster the increase experienced by ζ. Also, only cases V4 and V5 breach the extremality bound $\zeta = 1$. These cases are the ones in which $\chi_o > 1$ initially (see Table I). V4 becomes superextremal at a time $\sim 65M$ and V5 at $\sim 45M$. In both cases, ζ continues to grow until it reaches a maximum, at $\sim 85M$ for V4 and $\sim 70M$ for V5. The drop in ζ after reaching the maximum in V4 and V5 is due to the emission of angular momentum. The BH is not able to sustain superextremality and simultaneously retain axisymmetry.

Figure 4 also shows that after V4 and V5 reach a maximum, the ζ lines terminate. This signals the time when we are no longer able to locate the AH of the BH. We have investigated whether the loss of the AH is real or due to numerical effects. Simulations at different resolutions tells us that most likely the loss of the horizon is a numerical artifact: The last horizon times depend on resolution. The horizon undergoes a severe pancake deformation that the AH tracker is not able to handle because of the lack of resolution. We stress that the simulation does not crash; we only lose the horizon. This should not be viewed as "strange" since it is well known that stable puncture simulations do not resolve the puncture nor its immediate vicinity. If the horizon is too small, as with rapidly spinning BHs, the horizon is in danger of entering the underresolved region near the puncture.

Notice in Fig. 4 that for V4 around $150M$, when ζ becomes again subcritical, we are again able to find the AH, albeit only briefly. Although the value of ζ has significantly decreased, the shape of the horizon remains pancake-like, thus the challenge of locating the horizon remains. Since the AH shape is coordinate dependent, we

are currently investigating modifications to the puncture gauges that alleviate the horizon deformations, giving us a better chance of locating the horizon.

Finally, it is evident in Fig. 4 that ζ increases in the subextremal cases V2 and V3. V2 gives hints of reaching an asymptotic value at later times. On the other hand, V3 has an approximate linear growth between $75M$ and $300M$ when it saturates at $\zeta \sim 0.92$.

VI. NULL ENERGY CONDITION

As mentioned in Sec. II, one of the assumptions that the extremality condition $\zeta \leq 1$ hinges on is the validity of the null energy condition. The null energy condition states that for all null vectors k^a

$$\mathcal{N} = T_{ab}k^a k^b \geq 0. \tag{38}$$

Substitution in Eq. (38) of the stress-energy tensor T_{ab} with the form given by Eq. (33) yields

$$\mathcal{N} = \frac{2}{3}\rho - 2j_a l^a + M_{ab}^{TF} l^a l^b. \tag{39}$$

Above, we have used a null vector $k^a = n^a + l^a$ with $l^a n_a = 0$ and $l^a l_a = 1$. If we choose l^a to be radial and centered at the BH, i.e. $l^a = \hat{e}_r^a$, then

$$\mathcal{N} = \frac{2}{3}\rho - 2j_r + M_{rr}^{TF}. \tag{40}$$

We have evaluated (40) throughout the computational domain. Not surprisingly, we found that for all the negative energy density cases the null energy condition is violated in regions near the BH. Figure 5 shows snapshots for the cases V3, V4, and V5. The left panels in Fig. 5 are snapshots of the equatorial or $z = 0$ plane. The right panels are the $y = 0$ plane along the BH rotation axis. White areas are regions with positive values of $\mathcal{N}$, and gray shaded areas those in which the null energy condition is violated. The gray scale is logarithmic in absolute value, with minima of -2×10^{-4} for V3, -0.004 for V4, and -0.004 for V5.

The left panels in Fig. 5, showing the equatorial plane, make evident the formation of an inspiral (nonaxisymmetric) structure in $\mathcal{N}$ typically associated with BH accretion. Also interesting is that among the three cases depicted, only the one with the weakest negative energy shell, case V3, shows *no* region where the null energy condition is *not* violated. The right panels, $y = 0$ or edge-on planes, show hints of a double diagonal structure. They are a consequence of cutting through the "thick accretion disk" that forms. For the case V3, grid effects are also noticeable because of the small values that $\mathcal{N}$ takes.

We have also evaluated the null energy condition at the surface of the AH. That is, we evaluated $\mathcal{N}_H = T_{ab}k^a k^b$ on the AH using the null vector $k^a = n^a + s^a$, with s^a the
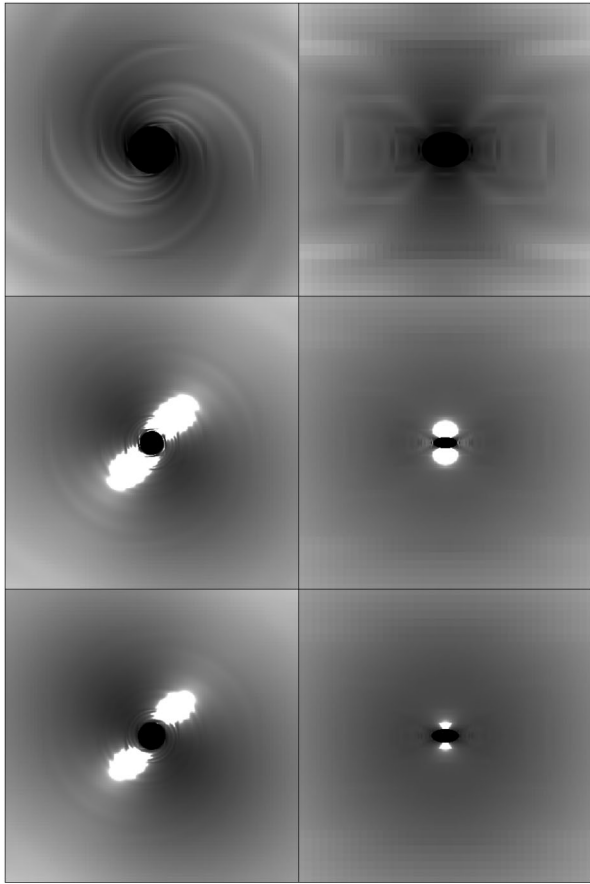
FIG. 5. Snapshots of $\mathcal{N}$ computed from Eq. (40). From top to bottom, cases V3, V4, and V5 are shown. They correspond to times $65.28M$, $62.72M$, and $50.24M$ for V3, V4, and V5, respectively, and cover a region $6M$ across. The left panels show a cut through the equatorial or $z = 0$ plane. The right panels show the $y = 0$ plane along the rotation axis of the BH. Gray shaded areas are those in which the null energy condition is violated. White areas in the V4 and V5 cases are regions with positive values of $\mathcal{N}$. The gray scale is logarithmic in absolute value, with a global minimum of -2×10^{-4} for V3, -0.004 for V4, and -0.004 for V5.

spatial unit normal to the AH. In Fig. 6, we show how the average of $\mathcal{N}_H$ changes during the course of the evolutions. The null energy condition is clearly violated in cases V2–V5. A closer look at the data shows that this null energy condition is violated not only on average, but also everywhere on the AH surface.

In summary, the violations of the null energy condition in the vicinity of the BH (Fig. 5) and on the surface of the AH (Fig. 6) demonstrate consistency with the violation of the extremality bound $\zeta = 1$.

VII. CONSTRAINTS AND LATE BEHAVIOR

To understand the late behavior and, in particular, to get clues about the instability of the superextremal BHs, we calculated the L2 norms of ρ, j^i, and $\mathcal{G}^i$ within concentric shells $1M < r < 2M$, $2M < r < 4M$, and $4M < r < 8M$ as a function of evolution time. Figures 7–9, show these
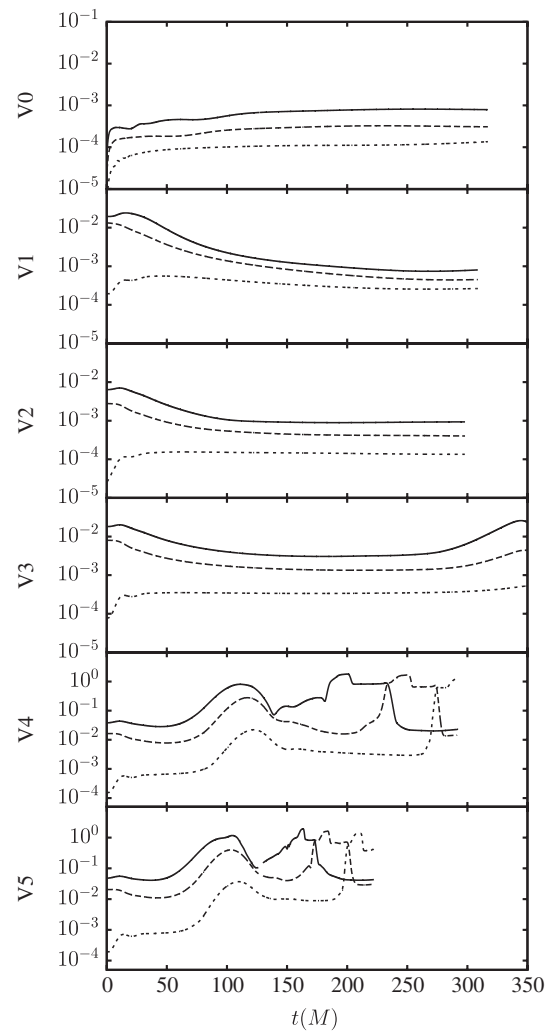

FIG. 6. Average of the null energy condition $\mathcal{N}_H$ on the surface of the AH.

FIG. 7. L2 Norm of ρ (right-hand side Hamiltonian constraint) in concentric shells: $1M < r < 2M$ (solid line), $2M < r < 4M$ (dashed line), and $4M < r < 8M$ (dotted line).
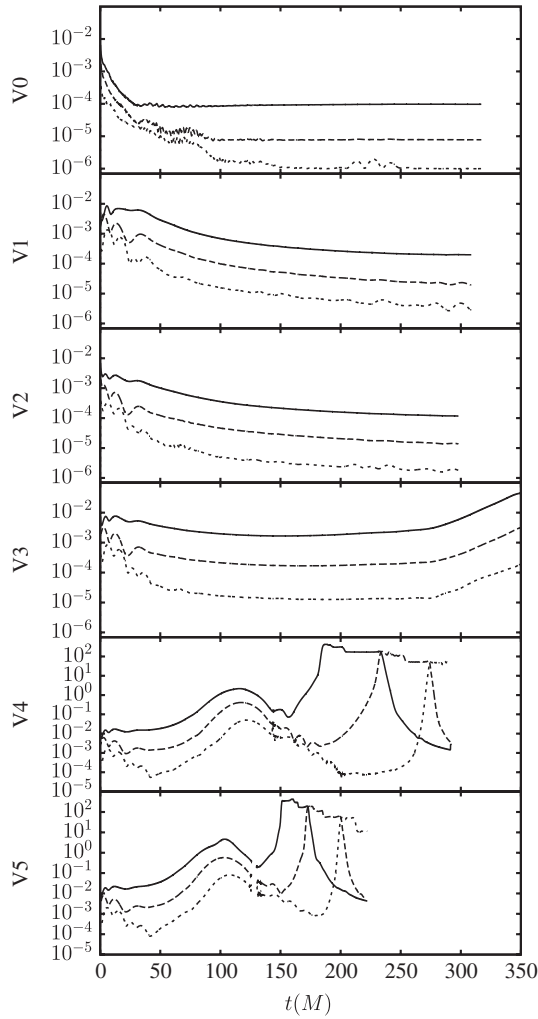
FIG. 8. L2 Norm of j^i (right-hand side momentum constraint) in concentric shells: $1M < r < 2M$ (solid line), $2M < r < 4M$ (dashed line), and $4M < r < 8M$ (dotted line).

FIG. 9. L2 Norm of the connection constraint $\mathcal{G}^a$ in concentric shells: $1M < r < 2M$ (solid line), $2M < r < 4M$ (dashed line), and $4M < r < 8M$ (dotted line).

L2 norms. First note that after $t \sim 100M$ the L2 norms of ρ, j^i, and $\mathcal{G}^i$ for the V0, V1, and V2 cases reach comparable levels. This signals that the V1 and V2 systems are settling down to a vacuum BH. Given that the BHs in V1 and V2 accreted matter, their final mass and spins will be different from those of V0.

Case V3 shows a different behavior. Initially, ρ, j^i, and $\mathcal{G}^i$ drop and stabilize as with V1 and V2 as a consequence of matter having been accreted by the BH. The approximately constant values are, however, larger than the corresponding values in V1 and V2. Beyond, $t \sim 250M$, ρ, j^i, and $\mathcal{G}^i$ begin to grow as the BH approaches its maximum ζ value at $t \sim 300M$ (see Fig. 4).

Cases V4 and V5, those that led to superextremal BHs, show more complex behavior. Initially, the slight drop of ρ, j^i, and $\mathcal{G}^i$ in the outer two shells gives a hint of the undergoing accretion with the inner shell remaining approximately constant. Around the time the BH surpasses
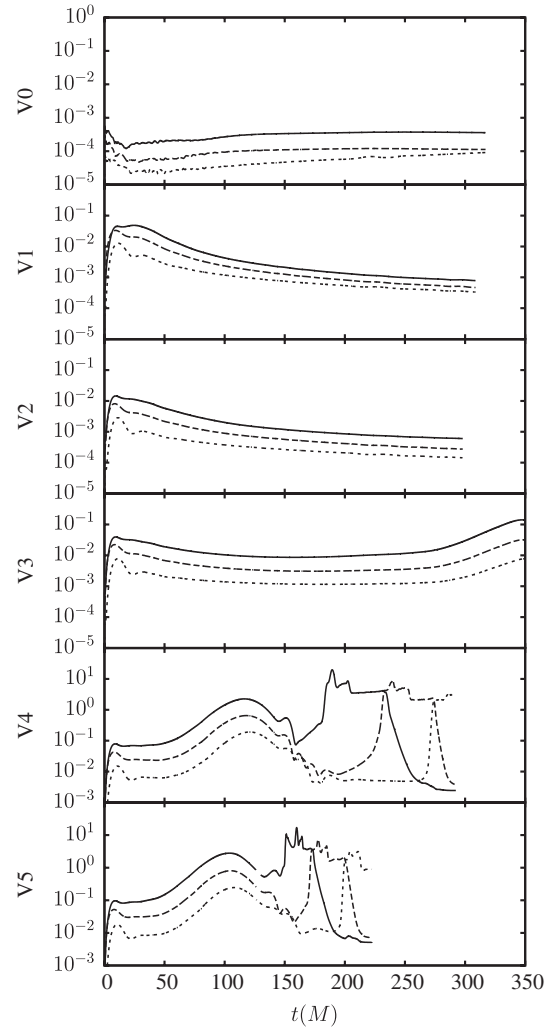
extremality, $t \sim 65M$ for V4 and $t \sim 45M$ for V5, ρ, j^i, and $\mathcal{G}^i$ start growing appreciably. This smooth growth continues until $t \sim 120M$ for V4 and $t \sim 100M$ for V5. During this period, ζ reaches a maximum value and proceeds to decrease. The decrease in ζ is eventually accompanied with a decrease in ρ, j^i, and $\mathcal{G}^i$. At around $t \sim 150M$ for V4 and $t \sim 130M$ for V5, an ejection burst is triggered deep in the interior of the BH. Evidence of this ejected burst is the delay at which the burst emerges in each of the shells. That is, in Figs. 7–9 the burst shows in the solid line first, dashed line next, and dotted line last.

The L2 norms in Figs. 7–9 do not provide a good sense of the details of the dynamics of ρ, j^i, and $\mathcal{G}^i$. In Fig. 10 we display the temporal evolution of spatial features. We show snapshots of ρ for the V4 case in the equatorial plane (left) and axis plane (right) at times $t \simeq 50M$, $100M$, $150M$, and $200M$ from top to bottom. The gray scale from top to bottom is such that [white:black] = [0: − 0.003],
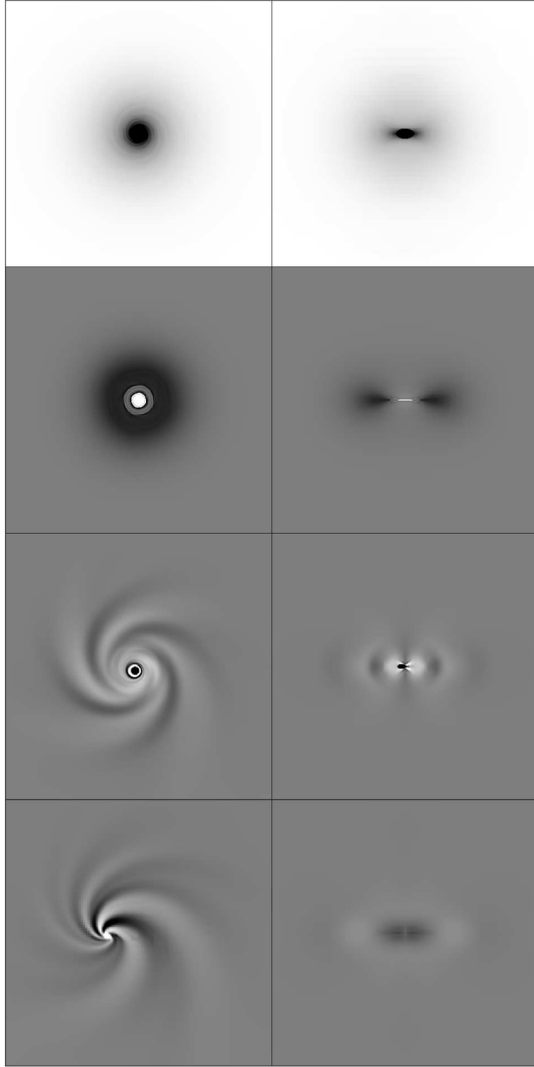
FIG. 10.   Snapshots of ρ of the V4 case in the equatorial-plane (left) and axis plane (right) at times $t \simeq 50M$, $100M$, $150M$, and $200M$. The gray scale from top to bottom is such that [white:black] = [0: − 0.003], [0.08: − 0.08], [0.02: − 0.02], and [0.008: − 0.008], respectively. The regions, all centered about the coordinate origin, are $5M$ across.

[0.08: − 0.08], [0.02: − 0.02], and [0.008: − 0.008] respectively. The panels are $5M$ across. The two bottom left panels clearly show a burst of negative energy. A similar burst is found in j^i, which explains the smaller value of ζ during a brief period at $t \sim 150M$ when the AH is again located. A detailed investigation of the late behavior of these superextremal cases will be the subject of subsequent study.

VIII. CONCLUSIONS

We have carried out a series of numerical experiments showing accreting BHs that violate the extremal spin condition $\zeta \leq 1$. The experiments consisted of a BH, modeled by a spinning puncture, surrounded by a spherically symmetric shell. We considered shells with positive energy density and negative angular momentum, but the main focus was shells with negative energy density and positive angular momentum. The idea behind this setup was that, as the BH accretes a negative energy, positive angular momentum shell, its mass will decrease and its spin will increase, leading to possible violations of the $\zeta = 1$ extremality bound. We were successful in violating the extremality bound, at least temporarily. In agreement with the findings by Booth and Fairhurst [6], the violations were accompanied with violations of the null energy condition. The BHs that violated the $\zeta = 1$ bound were not able to sustain superextremality and simultaneously retain axisymmetry.

Our results are also consistent with work by Jaramillo, Reiris, and Dain [16] that appeared soon after the submission of our manuscript. The work in Ref. [16] proved that $\zeta \leq 1$ holds for outermost stably marginally trapped surfaces that are axisymmetric in the presence of surrounding matter satisfying the dominant energy condition. The proof did not require axisymmetry of the exterior matter, only for the trapped surface.

Our study involved several challenges. The most significant challenge was locating the AH as the BH became superextremal. In subsequent work, we will investigate gauge conditions that could alleviate difficulties caused by the extreme deformations of the BH horizon. If a new gauge condition is found, we will be in a better position to investigate whether or not violations of extremality are accompanied with the disappearance of the AH. We will also focus on the late-time behavior to get a better understanding of the causes behind the late emission responsible for the drop of the spin parameter ζ.

Our study introduced a new approach to construct nonvacuum dynamical spacetimes: the *matter-without-matter* evolution framework. Under this approach, only the evolution equations are used, with the matter source terms set to zero. Specifically, we demonstrated that the $3 + 1$, BSSN vacuum evolution equations were capable of providing the dynamics of matter fields that are *invisible* to the equations. The price paid in MWM evolutions is restrictions on the "equations of state" satisfied by the matter content. It is not clear whether MWM evolutions could be applied to other $3 + 1$ formulations of the Einstein equations and produce stable and convergent simulations.

[1] M. Ansorg and H. Pfister, Classical Quantum Gravity **25**, 035009 (2008).

[2] J. Hennig, M. Ansorg, and C. Cederbaum, Classical Quantum Gravity **25**, 162002 (2008).

[3] J. Hennig, C. Cederbaum, and M. Ansorg, Commun. Math. Phys. **293**, 449 (2010).

[4] M. Ansorg and D. Petroff, Phys. Rev. D **72**, 024019 (2005).

[5] G. Lovelace, R. Owen, H. P. Pfeiffer, and T. Chu, Phys. Rev. D **78**, 084017 (2008).

[6] I. Booth and S. Fairhurst, Phys. Rev. D **77**, 084005 (2008).

[7] A. Ashtekar and B. Krishnan, Living Rev. Relativity **7**, 10 (2004).

[8] K. S. Thorne, Astrophys. J. **191**, 507 (1974).

[9] T. W. Baumgarte and S. L. Shapiro, Phys. Rev. D **59**, 024007 (1998).

[10] T. Bode *et al.*, Phys. Rev. D **80**, 024008 (2009).

[11] T. W. Baumgarte, S. A. Hughes, and S. L. Shapiro, Phys. Rev. D **60**, 087501 (1999).

[12] C. F. Sopuerta, U. Sperhake, and P. Laguna, Classical Quantum Gravity **23**, S579 (2006).

[13] J. Healy, P. Laguna, R. A. Matzner, and D. M. Shoemaker, Phys. Rev. D **81**, 081501 (2010).

[14] T. Bode, R. Haas, T. Bogdanovic, P. Laguna, and D. Shoemaker, Astrophys. J. **715**, 1117 (2010).

[15] D. Christodoulou, Phys. Rev. Lett. **25**, 1596 (1970).

[16] J. L. Jaramillo, M. Reiris, and S. Dain, arXiv:1106.3743.

[17] T. W. Baumgarte and S. L. Shapiro, *Numerical Relativity: Solving Einstein's Equations on the Computer* (Cambridge University Press, Cambridge, England, 2010).

[18] S. Brandt and B. Brügmann, Phys. Rev. Lett. **78**, 3606 (1997).

[19] J. M. Bowen and J. W. York, Jr., Phys. Rev. D **21**, 2047 (1980).

[20] J. W. York, Jr., in *Sources of Gravitational Radiation*, edited by L. L. Smarr (Cambridge University Press, Cambridge, England, 1979), p. 83.

[21] R. J. Gleiser, C. O. Nicasio, R. H. Price, and J. Pullin, Phys. Rev. D **57**, 3401 (1998).

[22] H. Bondi, Rev. Mod. Phys. **29**, 423 (1957).